Nanoscale

PAPER

View Article Online
View Journal | View Issue

Published on 28 July 2016. Downloaded by University of Texas Libraries on 11/21/2018 5:05:31 PM.

Cite this: *Nanoscale*, 2016, **8**, 15645

In situ growth of fluorescent silicon nanocrystals in a monolithic microcapsule as a photostable, versatile platform†

Guixian Zhu,[a,b] Yu Huang,[c] Gauri Bhave,[b] Yuzhen Wang,[b] Zhongbo Hu[a] and Xuewu Liu*[b]

Received 12th May 2016,
Accepted 26th July 2016

DOI: 10.1039/c6nr03829h

www.rsc.org/nanoscale

A facile, one-step method was developed for the *in situ* formation of fluorescent silicon nanocrystals (SiNC) in a microspherical encapsulating matrix. The obtained SiNC encapsulated polymeric microcapsules (SiPM) possess uniform size (0.1–2.0 μm), strong fluorescence, and nanoporous structure. A unique two stage, time dependent reaction was developed, as the growth of SiNC was slower than the formation of polymeric microcapsules. The resulting SiPM with increasing reaction time exhibited two levels of stability, and correspondingly, the release of SiNC in aqueous media showed different behavior. With reaction time <1 h, the obtained low-density SiPM (LD-SiPM) as matrix microcapsules, would release encapsulated SiNC on demand. With >1 h reaction time, resulting high-density SiPM (HD-SiPM) became stable SiNC reservoirs. SiPM exhibit stable photoluminescence. The porous structure and fluorescence quenching effects make SiPM suitable for bioimaging, drug loading and sorption of heavy metals (Hg^{2+} as shown) as an intrinsic indicator. SiPM were able to reduce metal ions, forming SiPM/metal oxide and SiPM/metal hybrids, and their applications in bio-sensing and catalysis were also demonstrated.

Introduction

Silicon-derived nanostructures (SiNC,[1] nanowires,[2] porous silicon,[3] *etc.*) have demonstrated excellent potential in the applications of photonics,[4–6] electronics[7–10] and biotechnology[11,12] owing to their unique photonic properties,[13] biocompatibility, readily available surface chemistry[14] and biodegradability.[15] Recently, SiNC have attracted research interest particularly for their unique luminescence properties as the result of a quantum confinement effect.[11] Compared to traditional fluorescent dyes and quantum dots, SiNC show better biocompatibility and fluorescence stability while eliminating toxic heavy metals contained in conventional quantum dots, which make SiNC promising for both *in vitro* and *in vivo* long-term bioimaging.[16] Various methods have been developed to produce SiNC, including the reducing inverse micelle method,[17] Zintl salts in inert organic solvents,[18] reduction of silane precursors by sodium metal,[19] laser pyrolysis of silane and plasma synthesis.[20] Surface modification strategies were also studied to tailor SiNC's hydrophobicity and surface charge to enrich functionalities and extend biomedical applications.[1] A few recent studies reported one-pot synthesis of amino modified SiNC by directly reducing aminosilanes.[15,21]

However, current applications of SiNC are quite limited. This is partially due to the constraints on size range of SiNC that can emit fluorescence. To achieve a quantum confinement effect, the SiNC size has to be in a narrow range near Si excitation Bohr radius.[11,22–24] Separation of small SiNC usually relies on a costly dialysis process or ultrafiltration centrifugal devices.[25]

Recent studies have attempted to overcome these issues by cross-linking SiNC into bigger nanoparticles,[26] or assembling existing SiNC inside larger structures, such as mesoporous organosilica[27] and polymers.[28,29] These hybrids integrated the properties of SiNC and a matrix to achieve synergistic effects, thus could greatly extend their potential in areas such as fluorescent probes, optics, photonics, catalysis and energy.[30] In addition, the supporting matrix may also form excellent SiNC storage to maintain robust photostability under harsh conditions.[31] However, due to the complexity of current procedures used for assembling SiNC hybrids, very few studies have been reported, and the application of SiNC has been limited to imaging. A simple method to synthesize SiNC containing microcapsules that may release SiNC on demand is desired to expand the field of SiNC applications.

[a]*College of Materials Sciences and Opto-Electronics, University of Chinese Academy of Sciences, Beijing 100049, China*
[b]*Department of Nanomedicine, Houston Methodist Research Institute, Houston, TX 77030, USA. E-mail: xliu@houstonmethodist.org*
[c]*Department of Biomedical Engineering, University of South Dakota, Sioux Falls, SD 57107, USA*

†Electronic supplementary information (ESI) available. See DOI: 10.1039/c6nr03829h

Published on 28 July 2016. Downloaded by University of Texas Libraries on 11/21/2018 5:05:31 PM.

Here, for the first time, we reported a single-step, highly efficient approach to simultaneously synthesize fluorescent SiNC contained in polymeric microcapsules by controlling the reaction of aminosilane and L-ascorbic acid (L-AA). The reaction was carried out in alcohol at room and mild temperature. While the resulting SiPM exhibit the typical fluorescence of SiNC, their sphere size (0.1–2.0 μm), fluorescence intensity, porous structure and stability are tunable by controlling the reaction conditions. Matrix microcapsules that will release SiNC in biological media can be synthesized. Taking the advantage of integrated properties of SiNC and porous structure of SiPM, we are able to develop a versatile platform for imaging, biosensing, catalysis, and removal of heavy metal contamination. The nanoporous structure and abundant amine groups make SiPM suitable in the sorption of heavy metals (Hg^{2+}), and the fluorescence intensity of SiNC inside can be used as a probe to monitor the amounts of heavy metals (Hg^{2+}) in SiPM. We also demonstrate that porous SiPM can reduce metal ions, forming SiPM/metal oxide (SiPM/MnO_2) and SiPM/metal composites (for example, SiPM/Au and SiPM/Pt), which show potential in bio-sensing and catalysis.

Results and discussion

Synthesis and characterization of SiPM

SiPM were synthesized by controlling the reaction of aminosilanes with L-AA. A proposed scheme of SiPM synthesis is illustrated in Fig. 1A. In a typical preparation, (3-aminopropyl)-trimethoxysilane (APTES) and L-AA (molar ratio [APTES] : [L-AA] ≈ 3 : 1) were used as starting materials to synthesize SiNC and polymer matrices. The reaction was carried out in isopropanol (IPA) containing a small portion (~5%) of water, which was essential for modulating the hydrolysis of APTES. A part of the APTES was hydrolyzed and condensed to form a siloxane-like polymer,[32–35] as illustrated in ESI eqn (S1),† while another part of the APTES was reduced by L-AA to yield SiNC.[36] L-AA was attached on the siloxane-like polymer mainly by non-covalent bonding (electrostatic adherence, *etc.*) or a hydrogen bond, which accelerated the formation of polymeric matrices. As the matrices condensed further, APTES, L-AA, and SiNC cross-linked into a larger spherical structure, which became a porous scaffold for further *in situ* growth of more SiNC. After this reaction, the SiPM were separated through centrifugation, and washed with IPA three times followed by storing in IPA.

Unlike the reported methods for preparing SiNC that involve microwave heating,[15,37,38] UV irradiation[21] or instant laser ablation,[39] our one-step synthesis method can be carried out by simply mixing starting materials in alcohol at room temperature. The obtained SiNC embedded microcapsules have uniform sizes ranging between 0.1–2.0 μm (prepared so far). The yield can reach about 60% in terms of Si content from the starting APTES. The as-prepared porous SiPM are positively charged, water dispersive, highly fluorescent, biocompatible and biodegradable.

Fig. 1B–E show typically synthesized porous SiPM, encapsulated SiNC and induced fluorescence. As shown in scanning electron microscopy (SEM, Fig. 1B) and transmission electron microscopy (TEM, Fig. 1C, inset) images, SiPM appear as uniform-sized spheres (1 μm shown, <10% variation by estimation). High-resolution TEM (HRTEM, Fig. 1C and S1†) images of SiPM (70 nm thin slices) show that SiNC (~2 nm in diameter) are uniformly distributed whose morphology and size are similar with results shown in previous studies, and the lattice spacing of the crystal is 0.31 nm, which matches the diamond lattice of Si (111). Elemental analyses of the SiPM (EDS, Fig. S2;† XPS, Fig. S3†) confirm the presence of Si, C, N and O. Both fresh SiPM and hydrolyzed SiPM are positively surface-charged (zeta potential, Fig. S4†), most likely due to the presence of a positively-charged amine group derived from APTES. This aminopropyl group becomes a side chain of polymer matrices after condensation. Similarly SiNC also show positive zeta potential (Fig. S4B†) due to the APTES surface coating. Positive charges are beneficial to keep SiPM dispersed in aqueous solutions. Fig. 1D shows absorption and photoluminescence spectra (PL) of SiPM. The broad absorption curve could be a result of light scattering of polymer matrices in SiPM. The as-prepared SiPM exhibit green fluorescence under UV irradiation. The inset shows captured photos of dispersed SiPM with and without UV irradiation at 365 nm. Fig. 1E shows N_2 adsorption/desorption isotherms of SiPM (24 h reaction time), showing a microporous structure. The pore-size distribution curve (inset) is obtained from the adsorption branch through the Dubinin–Astakhov (DA) method.[40]

Formation process of SiPM

In SiPM synthesis, formation of spherical polymer matrices and SiNC can be monitored through particle analysis and fluorescence measurement, respectively. A Beckman Multisizer 4 coulter counter was used to measure the size and concentration of SiPM (0.4–12 μm detectable range with 20 μm aperture). As shown in Fig. 2A and B, particle analysis has revealed a unique two-stage process. SiPM properties from two stages are distinctive. In the first stage (from beginning to about 1 h), both mean sphere size and amounts (sphere >0.4 μm) increase rapidly. Then both rates drastically drop by ~40 fold (calculated by comparing the slope of curves of each stage) after the first 1 h (starting second stage). During the second stage, there is no obvious change of size and amounts of SiPM. This drastic drop is likely due to the significant consumption of starting materials and the existence of critical concentration. However, if we change the concentration of starting APTES and L-AA, the size and yield of final SiPM are correspondingly affected. As seen in Fig. S5,† SiPM with a size range of 0.4–2.0 μm were successfully synthesized by varying the APTES concentration. By using other aminosilanes (such as *N*-(2-aminoethyl)-3-(trimethoxysilyl)propylamine or 2-[2-(3-trimethoxysilylpropylamino)ethylamino]ethylamine) instead of APTES, SiPM as small as 0.1 μm had been obtained. The photoluminescence intensity of SiPM at 500 nm (excitation

 This journal is © The Royal Society of Chemistry 2016

Published on 28 July 2016. Downloaded by University of Texas Libraries on 11/21/2018 5:05:31 PM.

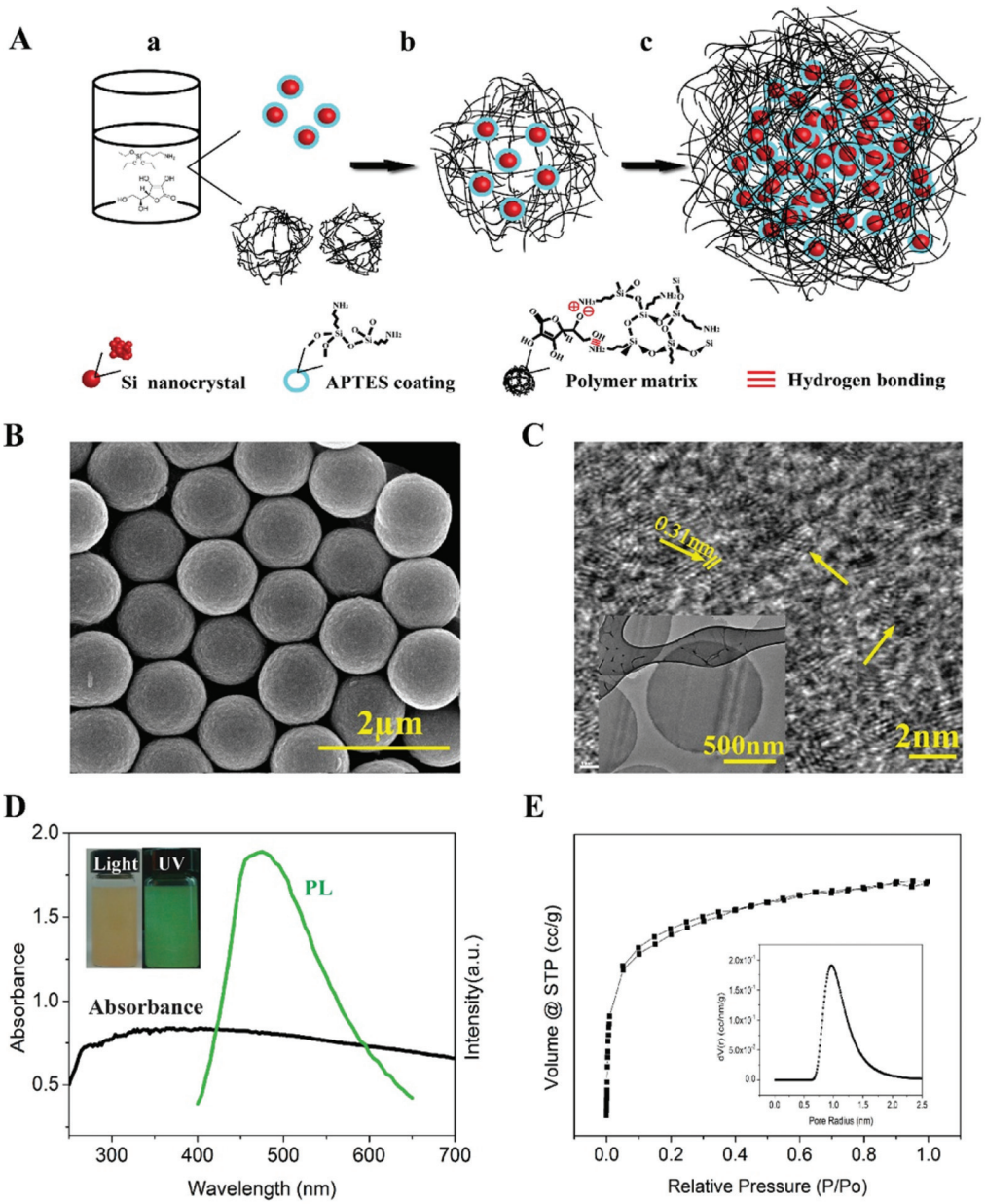

Fig. 1 (A) Proposed scheme of one-step synthesis of SiPM (a) L-AA reduce APTES to yield SiNC and hydrolyzed APTES to form siloxane-like polymer matrices; (b) formation of polymer matrices embedded with few SiNC; (c) spherical SiPM with more SiNC. (B) SEM image of typical synthesized SiPM (8 nm Pt/Pd sputtered). (C) TEM and HRTEM images of SiPM slices (70 nm thickness) cut with an ultramicrotome. (D) UV-vis absorbance and photoluminescence (PL) spectra of SiPM. The insets are pictures of dispersed solution of SiPM with and without UV irradiation at 365 nm. (E) N_2 adsorption/desorption isotherms of SiPM (24 h reaction time), the inset displays the Dubinin–Astakhov (DA) pore-size distribution curve obtained from the adsorption branch.

wavelength: 420 nm) also increased with the reaction time (Fig. S6†). However, unlike the trends observed for sphere size and amounts, the fluorescence intensity increased quite linearly in the first 2 h, then changed to a standard exponential curve of a first-order reaction (Fig. 2C). This means that the SiNC formation process saturates slower than the sphere formation, since fluorescence intensity represents the quantity of the encapsulated SiNC. A possible explanation is that SiNC continue to be reductively formed in pores. Even though spherical porous matrices are formed in 1 h, it takes longer for SiNC to fill the pores.

In the first stage, formation of siloxane-like polymer matrices is very fast and SiNC embedding is much slower, which results in a highly-porous, low density SiPM (LD-SiPM). Then the sphere formation slows down significantly to maintain a critical size and concentration, while the SiNC continue to be formed in the polymer matrices. Finally less porous, high density SiPM (HD-SiPM) were obtained. As shown in

Published on 28 July 2016. Downloaded by University of Texas Libraries on 11/21/2018 5:05:31 PM.

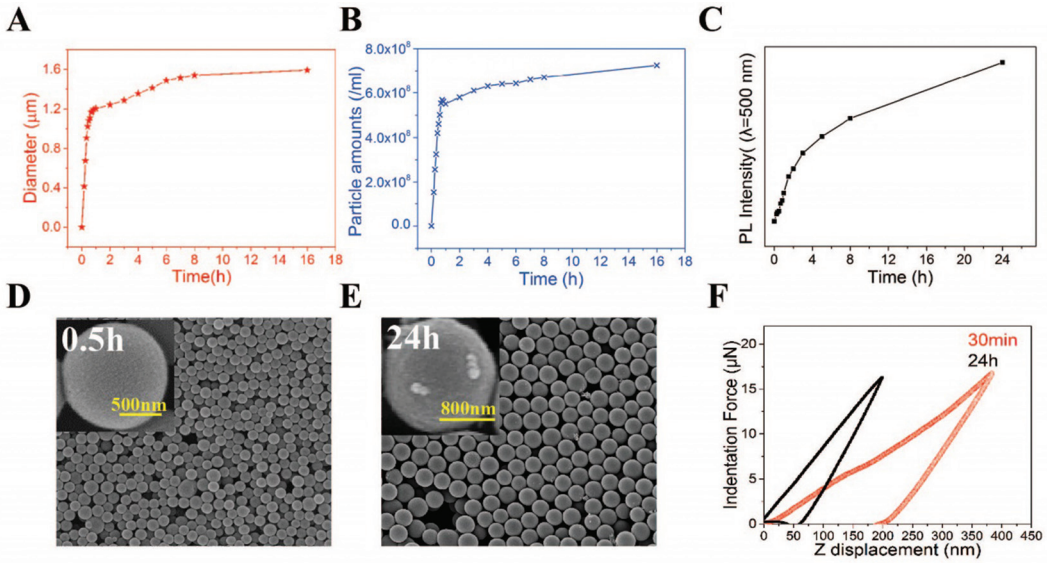

Fig. 2 Formation process of SiPM. (A) Change of mean size, and (B) particle concentration of SiPM with reaction time. (C) The change of fluorescence intensity of SiPM at λ = 500 nm (excitation wavelength: 420 nm) with reaction time. (D) SEM image of LD-SiPM (30 min reaction time); inset: zoomed-in image. (E) SEM image of HD-SiPM (24 h reaction time); inset: zoomed-in image. (F) The force–displacement curves for the LD-SiPM and HD-SiPM under the same indentation force.

Fig. 2D and E, LD-SiPM have a smooth appearance, while HD-SiPM show a nano-topographic structure possibly due to the clustered surface SiNC. The increase in hardness along with time is also verified *via* force–displacement curves (shown in Fig. 2F). Moreover, the solution color of HD-SiPM is darker than LD-SiPM (Fig. S7†). The elemental composition (Table S1†) also demonstrates an increasing ratio of Si in HD-SiPM. All these data indicate that SiNC continue to form in the second stage of the reaction with increasing time. More detailed SEM analysis of SiPM (Fig. 3) shows that soft siloxane-like polymer matrices are formed in the first 10 min, while during the next 10 min matrices are changed from an aggregated state to uniformly-sized spheres. Then, the color of the solution changes from ivory-white to light-yellow (without UV irradiation, shown in Fig. S8†), which indicates that SiNC embedding starts later than matrix formation and HD- and LD-SiPM exhibit distinctive porous structures. BET analyses of LD-SiPM after 30 min of reaction time and HD-SiPM after 24 h of reaction time (Fig. S9† and Fig. 1E) show mesoporous (~2.8 nm) and microporous (~0.9 nm) structure, respectively, indicating SiNC packing associated with reduced pore size in SiPM. As physical absorption specificity is heavily determined by the porous structures, two distinctive porous SiPM may perform differently in molecular absorption, which is under investigation.

SiNC releasing from SiPM

LD- and HD-SiPM are distinctive in hydrolytic degradability. The hydrolysis curves of both SiPM were calculated through recording PL spectra of released SiNC from microcapsules in DI water and Phosphate buffered saline (PBS), and are shown in Fig. 4A. Clearly, SiNC were released faster in PBS cell culture medium than in H_2O. In fact, the structure of LD-SiPM (reaction time 30 min) collapsed in 2 h, as 100% SiNC were released. However, HD-SiPM show higher stability, with less than 30% SiNC clustered nanoparticles (SiNP) falling off from SiPM. This is likely due to more complete cross-linking, denser SiNC packing, and smaller pore size. Fig. 4B shows residual of LD-SiPM after 24 h soaking in H_2O. Many SiNP (<100 nm) are found from the collapsed structure of microcapsules, which indicates unstable crosslinking of SiNP and siloxanes in capsules. The LD-SiPM dispensed solution becomes clear (Fig. 4C) in 24 h. LD-SiPM are able to be hydrolyzed in PBS as soon as in a few hours, depending on the reaction time (as seen in Fig. S10,† the hydrolysis time–reaction time curve). However, there is no obvious change for HD-SiPM. In order to quantify the hydrolytic behavior of HD-SiPM, a Multisizer was used to quantify the size and amounts of HD-SiPM during hydrolysis. Fig. 4D shows a decreasing trend for the diameter of HD-SiPM but without a corresponding decrease in particle amounts. There is much less SiNP fall off from HD-SiPM (Fig. 4E, inset SEM images and Fig. S11†), which is also in accordance with Multisizer results (the diameter of HD-SiPM changes from 1.6 μm to 1.39 μm) and the released curve measured by ICP-OES (Fig. S12†).

Compared with free-standing SiNC of a few nanometers, SiPM have several advantages due to their size. First, they are easy to handle. They can be collected, processed and stored through standard centrifugation and filtration processes. The microcapsule (LD-SiPM) can be used for SiNC storage, where SiNC can be released on demand. Second, nanopores in SiPM provide structural basis for absorption of molecules, making it possible for chemical detection,[41] catalysis,[42] drug delivery and controlled release. With their fluorescence, SiPM are also promising as fluorescent probes. Integration of these function-

 This journal is © The Royal Society of Chemistry 2016

Published on 28 July 2016. Downloaded by University of Texas Libraries on 11/21/2018 5:05:31 PM.

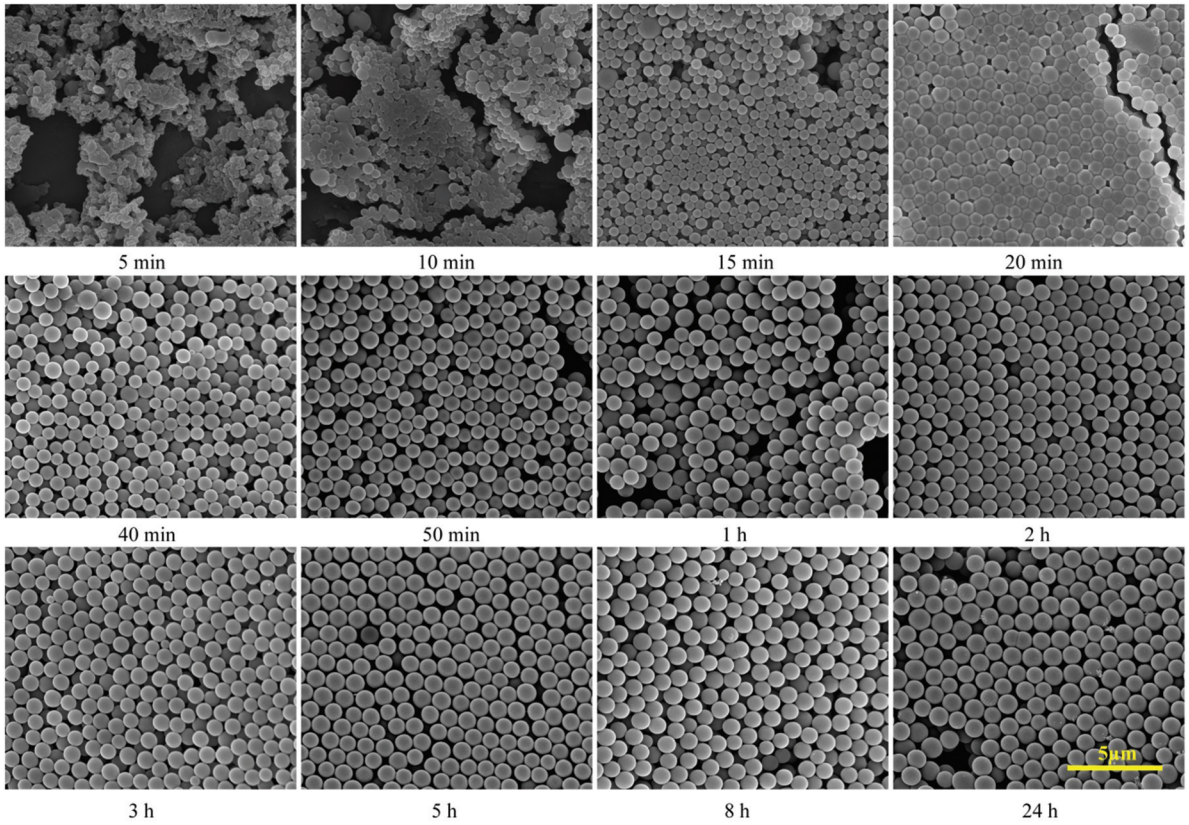

Fig. 3 SEM images of SiPM evolution with reaction times (5 min–24 h). Scale bar is 5 μm for all images.

alities opens broad opportunities, deserving further investigations. We explored the capability of SiPM to adsorb and reduce metal ions in aqueous solution, and confirmed that SiPM were able to reduce noble metal ions to generate metal oxides and metal nanoparticles in SiPM, which also indicates the existence of L-AA in SiPM. This also altered the fluorescence of SiPM. The resulting SiPM–metal hybrid particles may have potential applications in catalysis[43] and sensing.[44]

SiPM as a photostable fluorescent drug delivery vector

It is worth noting that gel-like siloxane-derived hybrids have also been reported with comparable fluorescence properties.[33,34,45] However, special treatments such as calcination[46,47] and instant ablation[39] are required for the synthesis. Based on our experiments, APTES in hydrochloric acid solutions formed ivory-white hybrids, but did not show fluorescence properties (data not shown). According to previous reports, carboxylic acids are critical for the formation of C substitutional defects for Si, to induce fluorescence in APTES-based hybrids.[48] These treatments are neither available nor needed for SiPM to trick the fluorescence. Moreover, SiPM lose their fluorescence if calcined in air, implying the effect of SiNC oxidation (data not shown). On the other hand, the emission spectrum of hydrolyzed products of SiPM (mainly composed of SiNC) is similar to that before hydrolysis. These suggest the embedded SiNC (rather than the polymer matrices) to be the source of fluorescence of SiPM.

Besides the quantum size effect of SiNC, the surface effects may also have an impact on their fluorescence.[11] The surface-capping molecules such as allylamine[49] and APTES[15] play an important role in the radiative combination mechanisms in 1–2 nm SiNC,[50] since their electronic charge distribution can be modified by the polar nature of their capping ligands. Therefore, the size and amine group on SiNC in SiPM are responsible for their fluorescence emission. SiPM exhibit strong fluorescence, and the quantum yield (QY) of released SiNC is similar to that of free SiNC (QY: ~20%, PL spectrum of quinine sulfate, as a reference, shown in Fig. S13†) prepared before,[36] and siloxane-like matrices do not seem to quench the fluorescence emission, making SiPM attractive for bioimaging. The photostability of SiPM and free SiNC was also evaluated under UV irradiation. As shown in Fig. 5A, the PL intensities of both samples continuously decreased along with illumination time. SiNC show a much faster decay rate than SiPM, and the remained PL intensity of SiNC decreased to 25% while the SiPM maintained a higher PL intensity value of 62%. We assessed submicron SiPM's fluorescence performance and biocompatibility for cell imaging. The cell uptake and intracellular behavior of SiPM by HeLa cells were also explored by monitoring green fluorescence (ex. 488 nm, em. 500–550 nm). To co-localize particles, DAPI and Alexa fluor

Published on 28 July 2016. Downloaded by University of Texas Libraries on 11/21/2018 5:05:31 PM.

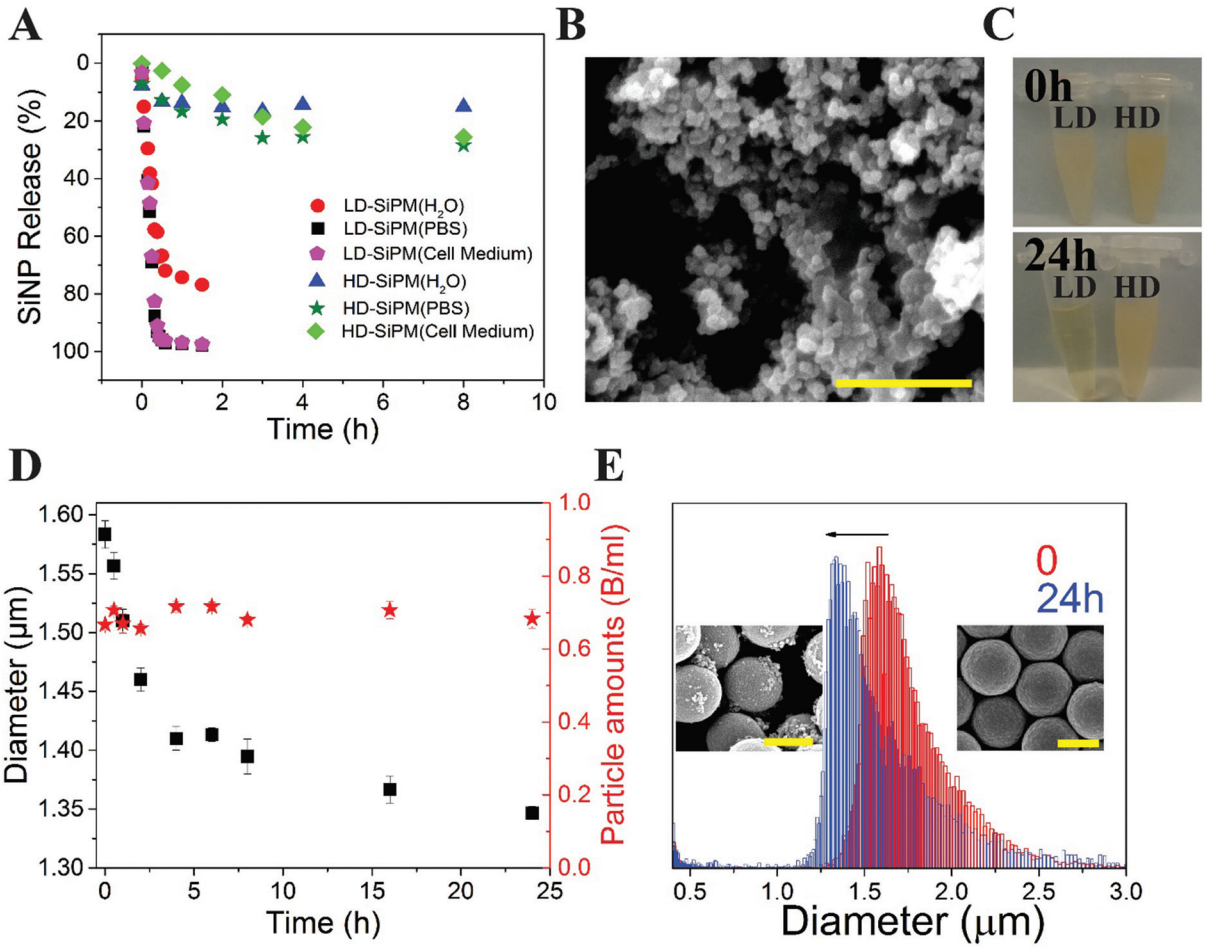

Fig. 4 Stability of SiPM with different reaction times in aqueous media. (A) SiNP release behavior from LD-SiPM (reaction time: 30 min) and HD-SiPM (reaction time: 24 h) in PBS, DI water and cell culture medium. (B) SEM image of the remaining SiNP/polymer matrix from LD-SiPM in H_2O. (C) Digital pictures of LD-SiPM (top, 30 min synthesis) and HD-SiPM (bottom, 24 h synthesis) immersed in PBS (pH = 7.4) for 0 h and 24 h. The LD-SiPM sample became clear in 24 h, indicating degraded substantial degradation, while the HD-SiPM sample showed little change. (D) Change of diameter and amount of HD-SiPM along with time in PBS. (E) Multisizer results of size distribution of HD-SiPM at the beginning and after 24 h immersion in PBS. The insets are SEM images of related HD-SiPM. Scale bar is 1 μm for all images.

555 Phalloidin were used for staining nuclei and actin respectively. The particles eventually accumulate in cytoplasm near cell nuclear envelopes after 4 h (Fig. 5B). In addition, nanopores in SiPM provides structural basis for absorption of molecules, making it possible for chemical detection,[41] catalysis,[42] drug delivery and controlled release. With their porosity, SiPM are also promising as bi-functional delivery vectors (for imaging and drug delivery).[51] We tested the loading of doxorubicin in SiPM, and the corresponding loading capacity is shown in Fig. S14.† SiPM demonstrate high biocompatibility with HeLa cells with over 95% viable cells after 24 h, even with a very high particle concentration (>1 million per mL SiPM) (Fig. 5C). When cells are incubated with SiPM/DOX and free DOX, concentration-dependent cell death is observed. Higher concentration of DOX would result in decrease of cell viability. The integration of these functionalities with fluorescence properties opens broad opportunities, deserving further investigations.

SiPM/MnO_2 hybrids for glutathione (GSH) detection

Glutathione (γ-L-glutamyl-L-cysteinyl-glycine; GSH), as the main non-protein thiol source, exists in most mammalian tissues.[52] It is necessary to monitor the level of glutathione due to its biological significance in diseases such as cancer,[53] HIV[54] and heart problems.[55] SiPM were able to *in situ* reduce $KMnO_4$ to MnO_2 sheets by immersing SiPM in $KMnO_4$ aqueous solutions (here we used HD-SiPM). The formed MnO_2 sheets were able to quench the photoluminescence of SiPM, which is recoverable when GSH was added.[56] The relationship between $KMnO_4$ amounts and quenching efficiency of the formed MnO_2 on SiPM is shown in Fig. 6A and B. The inset in Fig. 6B is a photo of the corresponding SiPM/MnO_2 solutions. MnO_2 formed by using 2 mM $KMnO_4$ in the reaction reached about 98% quenching efficiency on SiPM. The morphology of SiPM/MnO_2 slices (thickness: 70 nm) is observed through TEM (Fig. 6C). The morphology of SiPM is not significantly changed but on

 This journal is © The Royal Society of Chemistry 2016

Published on 28 July 2016. Downloaded by University of Texas Libraries on 11/21/2018 5:05:31 PM.

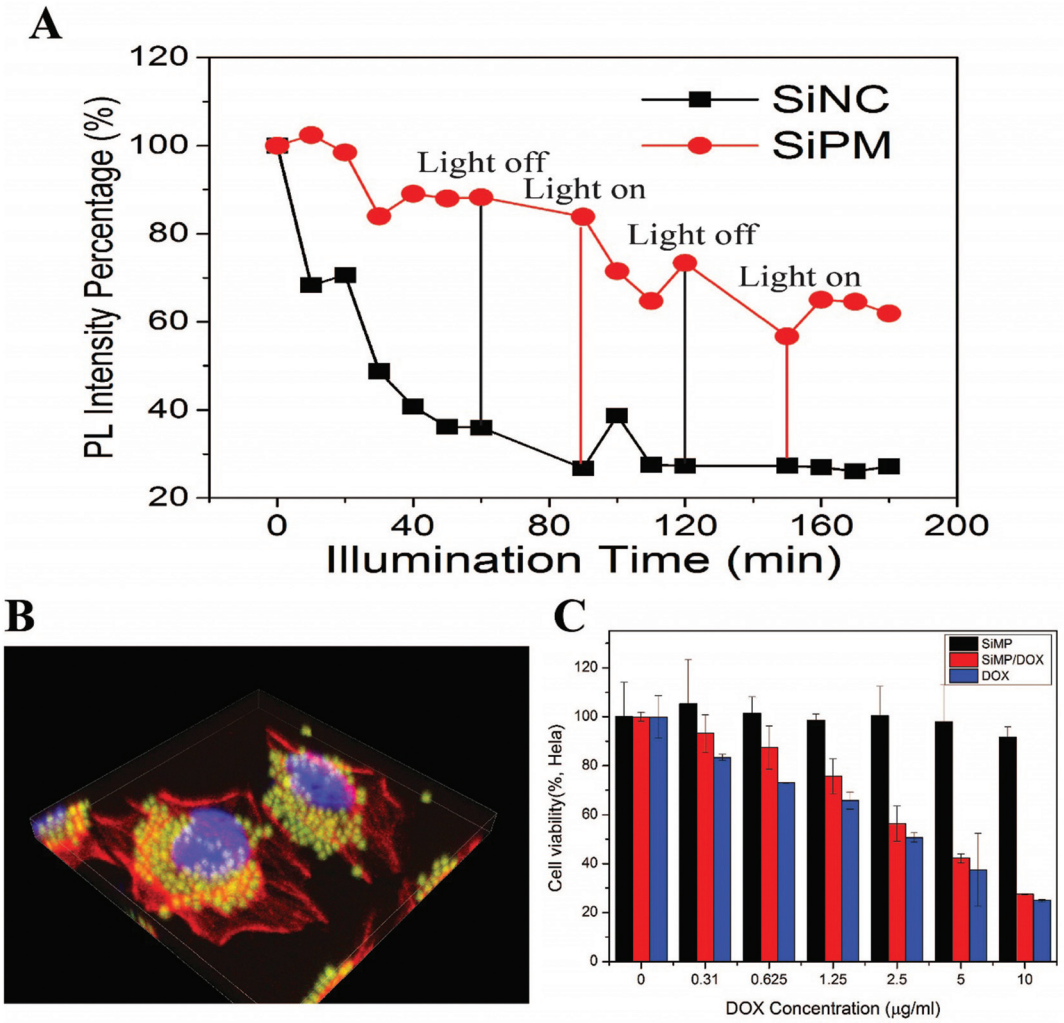

Fig. 5 (A) Remained PL emissions of Si nanoparticles and SiPM solutions along with increasing illumination time (Rayonet-600 photochemical reactor, 120 W). (B) 3D confocal image of HeLa cells after incubation with SiPM for 4 h. (C) Cell viability of HeLa cells after 24 h incubation with free DOX, SiNP and SiNP/DOX of various concentrations DOX. Results are the average from three independent experiments.

enhanced contrast. The existence of Mn on SiPM/MnO_2 is also verified by EDS (Fig. S15†). The recovery of photoluminescence is realized through a redox reaction between MnO_2 in SiPM and GSH, and the fluorescence spectra of this process is shown in Fig. 6D. The amount of photoluminescence that is recovered is proportional to the GSH concentration. It is noted that there is hardly any fluorescence recovery for the control sample in Fig. 6D compared with other samples (with GSH addition). Therefore, SiNC release causes little influence on final results. The limit of detection (LOD) is adjustable by changing the amounts of $KMnO_4$ in the reaction and SiPM/MnO_2 in detection.

HD-SiPM applied in Hg^{2+} sorption

Mercury is one of the poisonous heavy metals where the residual level of its ionized form (Hg^{2+}) in drinking water remains a big problem for environmental science and pollution research.[57] Though amine terminated SiNC had been used as a fluorescent probe in detecting Hg^{2+} in aqueous solutions *via* the affinity of Hg^{2+} to N,[58] previously used SiNC is dissociated, lacking the capability to deplete Hg^{2+}. In contrast, the highly nanoporous structure in our SiPM is suitable for adsorbing molecules. A detection–sorption multiplexed platform of Hg^{2+} was developed by integrating the porous structure and fluorescence of SiPM. The adsorption curve of Hg^{2+} at different concentrations by using SiPM is shown in Fig. 7A. HD-SiPM show high adsorption capacity and more than 300 mg Hg^{2+} can be adsorbed in 1 g SiPM. Also the adsorption process is highly efficient, usually saturated within 1 min, thus the small release of SiNC hardly affects detection accuracy. The relative fluorescence quenching efficiency of Hg^{2+} on SiPM is shown in Fig. 7B. 10^{-3} M Hg^{2+} shows about 50% fluorescence quenching on the photoluminescence spectrum of SiPM, which, however, can be recovered with GSH addition (10^{-3} M). The nanoporous structure of SiPM is responsible for adsorbing Hg^{2+}, while SiNC in SiPM act as a fluorescent probe for moni-

Published on 28 July 2016. Downloaded by University of Texas Libraries on 11/21/2018 5:05:31 PM.

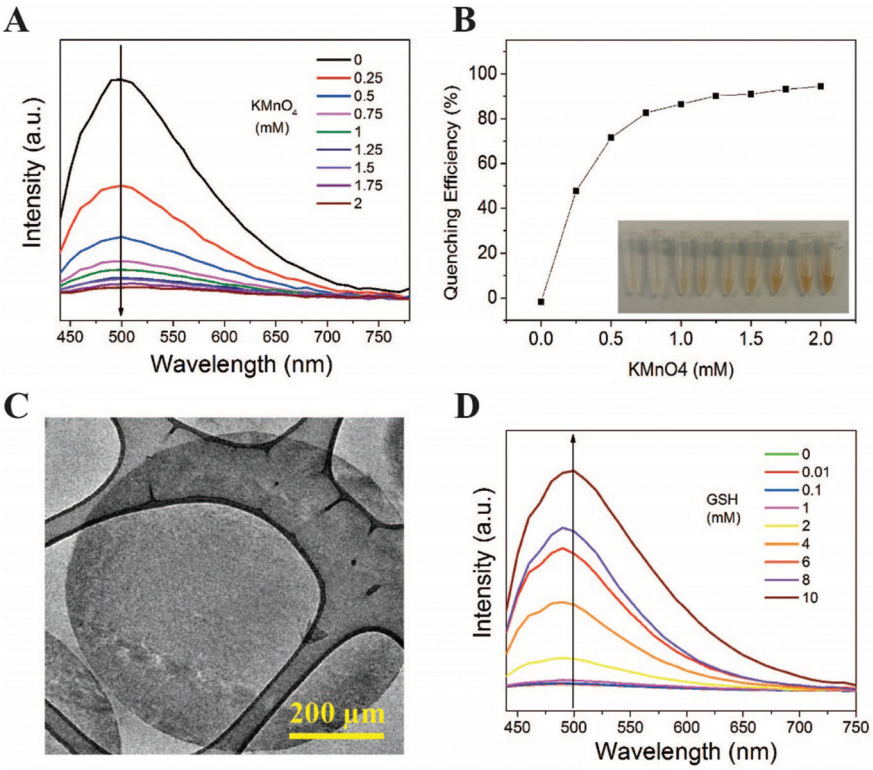

Fig. 6 Bio-sensing by using the SiPM/MnO_2 composite. (A) Photoluminescence spectra (excitation wavelength: 420 nm) of SiPM/MnO_2 resulting from various concentration of $KMnO_4$ in reaction. (B) The quenching efficiency of MnO_2 on SiPM along with increasing concentration of $KMnO_4$; the inset is captured images of the corresponding SiPM/MnO_2 composites. (C) TEM image of SiPM/MnO_2 composite slices (thickness: 70 nm). (D) The fluorescence spectra (excitation wavelength: 420 nm) of SiPM/MnO_2 (SiPM reacted with 2 mM $KMnO_4$) with increasing GSH concentration.

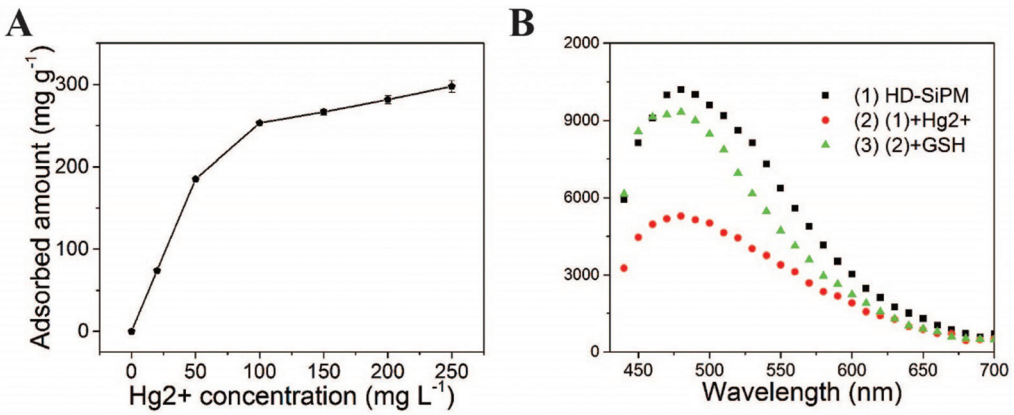

Fig. 7 (A) Adsorption curve of Hg^{2+} at various concentrations by using HD-SiPM. (B) The fluorescence spectra (excitation wavelength: 420 nm) of SiPM before (black) and after addition of Hg^{2+} (1 mM, red) and after addition of GSH (green).

toring adsorbed Hg^{2+}. The detection–sorption multiplexed platforms are recyclable simply by using GSH to recover Hg^{2+} from the SiPM.

SiPM/Au/Pt composites for catalyzing 4-nitrophenol (4-NP)

The SiPM were proven to reduce noble metal ions into nanoparticles from their aqueous solutions due to the existence of L-AA in SiPM. In our SiPM, we show that reduction can happen *in situ* at the nanopores. Here we demonstrate that the resulting silicon–metal nano-composite can be used for catalysis of a redox reaction. Fig. 8A shows a TEM image of SiPM/Au. The distribution of Au nanoparticles (AuNP) in SiPM seems to match the porous structure in SiPM. AuNP are mostly seen on the outer surface, and there is a blank shell portion where no

 This journal is © The Royal Society of Chemistry 2016

Published on 28 July 2016. Downloaded by University of Texas Libraries on 11/21/2018 5:05:31 PM.

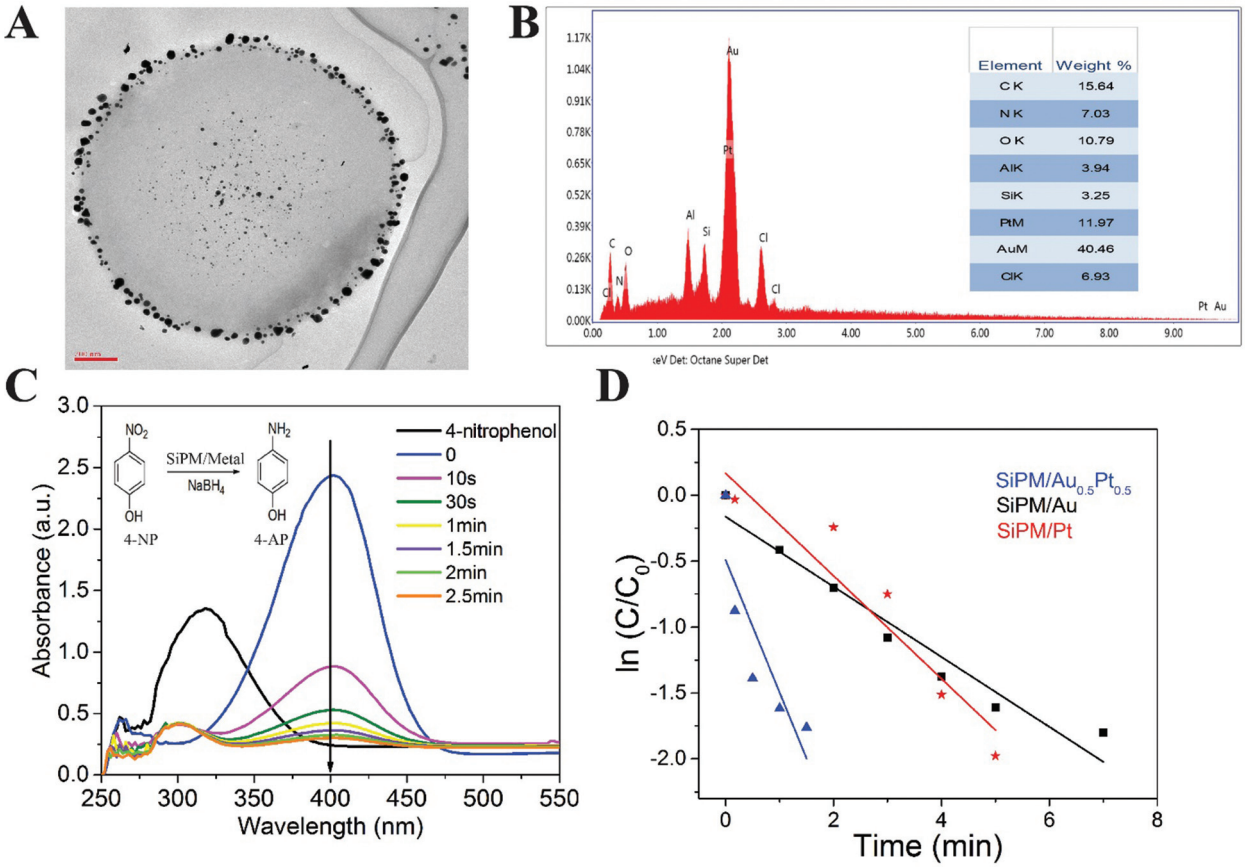

Fig. 8 (A) TEM image of SiPM/AuNP slices (70 nm thin), indicating SiPM reduced gold ions to form AuNP (dark-phased black particles) throughout the SiPM matrix. (B) EDS spectrum of SiPM/$Au_{0.5}$/$Pt_{0.5}$; the inset is elements' composition. (C) UV-vis spectra during catalytic conversion of 4-NP by SiPM/$Au_{0.5}$/$Pt_{0.5}$ over time; the inset is principle of reduction of 4-NP by $NaBH_4$ to form 4-AP. (D) $\ln(C/C_0)$ *versus* *t* for the reduction of 4-NP catalyzed by SiPM/Au, SiPM/Pt and SiPM/$Au_{0.5}$/$Pt_{0.5}$.

AuNP are visible. There are also AuNP visible at the center, indicating SiNC are also nucleated deeply in SiPM through diffusion of ions. Fig. 8B, S16 and S17† show EDS spectra of SiPM/$Au_{0.5}$/$Pt_{0.5}$, SiPM/Au and SiPM/Pt (HD-SiPM were applied). The reduction of 4-nitrophenol (4-NP) to 4-aminophenol (4-AP) by $NaBH_4$ was used to examine the catalytic activity of SiPM/metal composites.[59] Fig. 8C shows catalytic conversion of 4-NP by SiPM/$Au_{0.5}Pt_{0.5}$ and the inset is the principle of reduction. The absorption peak of 4-NP was at 317 nm and red-shifted to 400 nm after $NaBH_4$ was added, due to ionization of 4-NP. When the SiPM/metal composites were added, the color of the reacting solution changed from bright yellow to colorless, which reflects the diminishing absorption at 400 nm. The reaction rate can be evaluated *via* slope of kinetic curves since concentration of $NaBH_4$ was excessive compared with that of 4-NP. Fig. 8D shows a change of $\ln(C/C_0)$ along with the reaction time. The plots can be linearly fitted by the equation: $\ln(C/C_0) = kt$. C and C_0 stand for reactive and initial absorbance intensity at 400 nm. k stands for the rate constant, which can be used to calculate catalytic ability of these composites.[59] SiPM/$Au_{0.5}Pt_{0.5}$ (k = 0.492) demonstrate the highest catalytic ability compared to SiPM/Au (k = 0.162) and SiPM/Pt (k = 0.168). Reducing metal ions (Cu, Pt, Ag and Au verified) to form SiPM/metal composites greatly extends the potential application of SiNC in applications such as detection, antibiosis, Surface Enhanced Raman Scattering (SERS) and drug delivery.

Chemical composition analysis of SiPM

The organic composition of SiPM is mostly APTES derived siloxane-like polymer (eqn (S1)†). The chemical structures are confirmed by the diverse spectroscopies. The FTIR (Fig. S18†) exhibits characteristic peaks of Si–O–Si from siloxane-like backbone, C–H stretching, O–H stretching, stretching and bending of the N–H bond, and potential C=C and C=O stretching vibrations, suggesting the existence of L-AA in polymeric matrices. The NMR spectrum further confirms the existence of both APTES-derived siloxane-like polymer and L-AA (Fig. 9A), with the peaks at 2.9, 1.7 and 0.6 ppm corresponding to the propyl group in APTES, and it is significant to note the loss of up to three ethoxy groups for APTES during coupling of molecules in forming polymer matrices and to surfaces of silicon nanoparticles.[49,60] For recording the NMR spectrum of L-AA, "D_2O shake" occurs when using D_2O as a solvent in NMR

Published on 28 July 2016. Downloaded by University of Texas Libraries on 11/21/2018 5:05:31 PM.

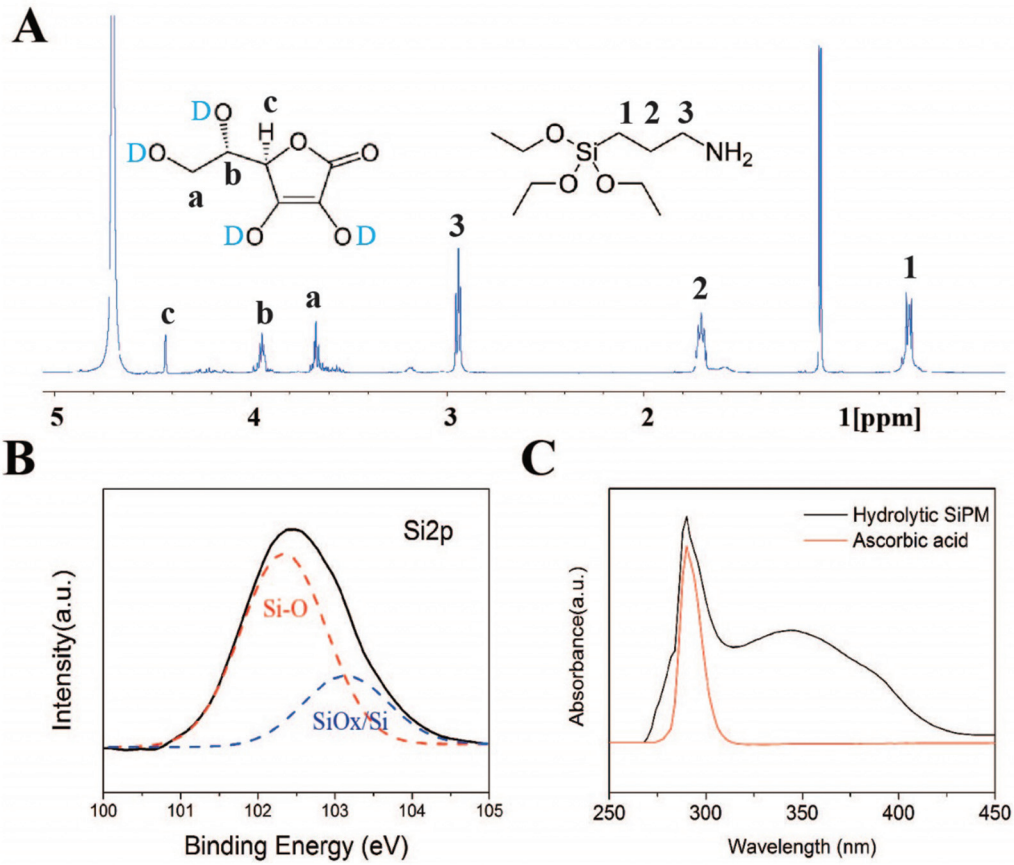

Fig. 9 (A) Solution-phase 1D ^{1}H NMR spectrum of hydrolytic SiPM in D_2O. (B) Structure analysis of high resolution XPS spectra: Si 2p. (C) UV-vis absorption spectrum of hydrolytic SiPM and L-ascorbic acid.

testing, in which the exchangeable protons are exchanged with the deuterium in D_2O and disappear in the spectrum.[61] The patterns at 3.7 and 3.9 ppm are distinguished as the $-CH_2$ group linked with hydroxyl in L-AA. The signal at 4.4 ppm is attributed to the proton on the heterocycle. A sharp peak observed at 1.1 ppm is due to the residue of IPA molecules in the samples. In the 2D-TOCSY spectrum (shown in Fig. S19†), one set shows typical correlation and chemical shift of the propyl group in APTES, while the other set matches well with that of L-AA. The resonance of the former set is roughly two times stronger than the latter one, suggesting less abundance of L-AA in matrices. This is consistent with elemental analysis and zeta potential measurements. There are two facts worthy of note. First, no protons from ethyloxy groups are observed, suggesting that APTES is mostly hydrolyzed during condensation.[49,60] Second, neither short- nor long-range coupling is observed between APTES-derived siloxane and L-AA. This suggests that the incorporation of L-AA in the siloxane-like backbone could be through non-covalent bonding (electrostatic adherence *etc.*) or a hydrogen bond. The high resolution XPS spectra (Fig. S3† and Fig. 9B) indicate chemical bonds of C–C, C–N, C–O, C═O and Si–O in SiPM. While the existence of C–C, C–N and NH_2 is attributed to the aminopropyl side chain, the Si–O is attributed to the siloxane-like backbone. Fig. 9C shows the UV absorbance curve of hydrolytic SiPM as compared to control of L-AA. (Note: the peak at around 350 nm is attributed to SiNC.) Both curves have a consistent sharp absorption at around 300 nm, suggesting that L-AA is preserved in polymer matrices.

Conclusions

In summary, we developed a one-step method for facile, highly efficient synthesis of SiNC contained in microcapsules. The as-prepared SiPM show uniform morphology, great aqueous dispersibility, strong photoluminescence, and porous structure. The size, yield, porosity, fluorescence intensity, and stability of SiPM are adjustable by simply changing reaction parameters. The combination of fluorescent SiNC and highly porous polymeric matrix makes SiPM an excellent self-indicator in adsorption of Hg^{2+} in aqueous solution. SiPM can also reduce metal ions in their aqueous solution and alter their fluorescence. The formed SiPM/MnO_2 and SiPM/$Au_{0.5}/Pt_{0.5}$ show excellent performance in detecting GSH and catalytic activity of 4-NP. These SiPM/metal oxide and SiPM/metal nanoparticles can be applied in areas such as cancer therapy,[62] biosensors[44] and catalysis.[43]

 This journal is © The Royal Society of Chemistry 2016

Published on 28 July 2016. Downloaded by University of Texas Libraries on 11/21/2018 5:05:31 PM.

Experimental

Materials

(3-Aminopropyl)-trimethoxysilane (APTES, 99%), L-ascorbic acid (L-AA, 99%), isopropanol (IPA), hydrogen tetrachloroaurate(III) hydrate ($HAuCl_4$), silver nitrate ($AgNO_3$), potassium permanganate ($KMnO_4$), mercury(II) chloride and quinine sulfate were purchased from Sigma-Aldrich. All chemicals were used without additional purification.

Synthesis and characterization of fluorescent SiPM

Silicon nanocrystals (SiNC) containing polymer microcapsules (SiPM) were synthesized by controlling the reaction of APTES and L-AA. Typically, 100 μL APTES and 1.5 mL of 0.1 M L-AA aqueous solutions were added into 30 mL IPA. The mixture was briefly sonicated, and then kept at a specific temperature for a defined time. The reaction can be carried out at room temperature, however, it is accelerated and getting better control at mild temperature. The SiPM demonstrated in this paper were synthesized at 60 °C. Typical fluorescent SiPM with ~1 μm diameters were then obtained. After the reaction, the SiPM were first precipitated through centrifugation at 10 000*g* for 5 min, washed three times using IPA and then stored in IPA. Scanning Electron Microscopy (SEM, high vacuum, HV = 8 kV, spot size 3.5), JEM-2100 Field Emission Gun Transmission Electron Microscope (TEM), X-ray Photoelectron Spectroscopy (XPS) and EDS were utilized for characterizing the structure, morphology and elements of the prepared SiPM. The surface chemical band was monitored by Fourier Transform Infrared Spectroscopy (FTIR) and XPS. Malvern Zetasizer was used to assess zeta potential of SiPM. The composition of the polymer matrix was tested by 1D ^1H NMR and 2D TOCSY NMR. SiPM (reaction time, 20 min) were hydrolyzed in D_2O. The hydrolytic sample was added into the NMR tube and measured by 600 MHz NMR.

Tuning the size, yield, fluorescence intensity, porosity and biodegradability/hydrolysis of SiPM

The influence of reaction time on the size of SiPM was explored. Briefly, after mixing APTES with L-AA in IPA, the mixture was allowed to react for various times (from 30 min to 24 h) and then the reaction was terminated by washing. In order to test the effect of reagent concentration on the final size of SiPM, 100 μL APTES and 1.5 mL 0.1 M L-AA aqueous solutions were added in IPA of different volumes (from 15 mL to 180 mL). The Multisizer 4 Coulter Counter (Beckman Coulter) was used to monitor the change of size and count of the as-prepared SiPM. The impact of reaction time on fluorescence intensity of SiPM was investigated by measuring their photoluminescence curves by using a Synergy H4 Hybrid Reader (Bio TEK). N_2 adsorption/desorption isotherms of different samples were measured using a Quantachrome Automated Gas Sorption Analyzer, and the surface area and pore size distribution were calculated by Dubinin–Astakhov (DA) and Barrett–Joyner–Halenda (BJH) methods.

In order to evaluate the SiNP release behavior from LD-SiPM and HD-SiPM, one billion SiPM are immersed in 500 μl DI water and PBS respectively. The dispensed solutions were centrifuged at different time points, and the PL spectra of the supernatant (SiNP) were recorded *via* a plate reader. The precipitate was tested by SEM and Multisizer to monitor their morphology, size and amounts.

To test biodegradation kinetics of Si, 1.25×10^{10} SiPM (n = 3) were dispersed into 500 μL PBS (pH = 7.4). The mixtures were kept in the Digital Heatblock at 37 °C. At different time points, 10 μL SiPM solution was taken out and centrifuged, and the precipitate was extensively washed using IPA and centrifuged at 13 000*g* three times, then spotted on an SEM stub for imaging their morphology change. At the same time point, SiPM were spun down, and the supernatant was replaced with 500 μL fresh PBS. All the supernatant was collected and diluted in DI water, and stored at 4 °C for following Si element analysis, which was measured by using an Inductively Coupled Plasma Optical Emission Spectrometer (ICP-OES, Varian 720-ES).

SiNC are produced according to a previous method.[36] Briefly, 100 μL APTES is mixed with 1 mL of 0.1 M L-AA and reacts for 1 h. The residual reagents were removed by dialysis (1 kDa). The resulting SiNC exhibit green fluorescence under UV irradiation.

The quantum yield of SiNC and release of SiNC from SiPM were determined by using quinine sulfate as a standard, and QY values are based on the established equation: $Q_x = Q_r M_x N_x^2/(M_r N_r^2)$.[21,63] N, M, and Q stand for the average refractive index of the solvent, the gradient of straight line, and quantum yield. r and x indicate the reference quinine sulfate and the tested SiNC, respectively. The values of optical densities at the excitation wavelength of samples were adjusted to the same values (≤0.1).

CCK-8 assay and cell uptake of SiPM

The human cervical cells HeLa were cultured in Dulbecco's modified Eagle's medium (DMEM) supplemented with 10% fetal bovine serum (FBS) and antibiotics (100 μg mL^{-1} streptomycin and 100 U mL^{-1} penicillin). Both cell lines were cultured under the conditions of 5% CO_2 and 95% humidity at 37 °C.

Suspensions of 1×10^5 cells per mL HeLa were plated in Lab-Tek Chamber Slides (Thermo Fisher Scientific, USA) and cultured overnight, followed by adding SiPM (2.5×10^6 mL^{-1}). They were cultured for 1 h and 4 h separately. After washing using PBS 3 times, the cells were fixed with 4% glutaraldehyde in PBS for 30 min at room temperature. The fixed cells were stained with DAPI before observing by using a Nikon A1 Confocal Imaging System. Counting Kit-8 (CCK-8) assay was applied to evaluate cytotoxicity. Briefly, 1×10^4 HeLa cells were plated separately in 96-well plates and cultured overnight. Then they were exposed to SiPM, SiPM/DOX and free DOX with various concentrations for 24 h. After 4 h of 10 μL CCK-8 addition, the absorption peak of medium at 450 nm and 630 nm by using a Synergy H4 Hybrid Reader (Bio TEK).

Published on 28 July 2016. Downloaded by University of Texas Libraries on 11/21/2018 5:05:31 PM.

Synthesis of SiPM/MnO_2 for detecting glutathione (GSH) in aqueous solutions

SiPM/MnO_2 composites were synthesized by simply mixing SiPM with $KMnO_4$ aqueous solutions. Briefly, various volumes of 40 mM $KMnO_4$ were added in SiPM dispensed aqueous solution (with about 1×10^8 SiPM), and reacted for 2 h. After the reaction, the formed SiPM/MnO_2 was collected *via* centrifugation at 10 000*g* for 5 min, washed using IPA three times and then stored in IPA. In order to test GSH detection using SiPM/MnO_2 composites, GSH solutions at different concentrations were added into SiPM/MnO_2 composite solutions. The change of photoluminescence spectra was recorded by using a plate reader.

SiPM applied in Hg^{2+} adsorption

The stock solution of 1000 ppm of Hg^{2+} was prepared by dissolving 13.54 mg $HgCl_2$ in 10 mL DI water. 10 μL of 1 B per mL HD-SiPM were mixed with Hg^{2+} at different concentrations. The PL spectra of SiPM/Hg^{2+} were recorded by using a plate reader. After 5 min, the supernatant was collected *via* centrifugation and measured by ICP-OES to calculate Hg amounts inside.

Synthesis of SiPM/Au, SiPM/Pt and SiPM/$Au_{0.5}Pt_{0.5}$ for catalytic activity on 4-nitrophenol

For SiPM/Au, briefly, 30 μL of 20 mM $HAuCl_4$ was added into SiPM dispensed aqueous solution (with about 1×10^8 SiPM), and reacted for 24 h. 2 μL of 300 mM K_2PtCl_4 was reacted with SiPM for the formation of SiPM/Pt. For SiPM/$Au_{0.5}Pt_{0.5}$, 15 μL of 20 mM $HAuCl_4$ and 2 μL of 300 mM K_2PtCl_4 were simultaneously mixed with SiPM solutions. After the reaction, the formed composites were collected *via* centrifugation at 10 000*g* for 5 min, washed using IPA three times and then stored in IPA.

The reduction of 4-nitrophenol (4-NP) by $NaBH_4$ was used to test the catalytic activity of SiPM/metal composites in aqueous solutions. Briefly, 2 μL of 0.1 M 4-NP and 10 μL of 1 M $NaBH_4$ were added into 2 mL DI water in a cuvette. Then 80 μL of SiPM/metal (SiPM/Au, SiPM/Pt and SiPM/$Au_{0.5}Pt_{0.5}$) composites were added into the cuvette. The UV-vis spectrometer was used to record the change of absorbance curves along with time.

Acknowledgements

The authors would like to thank Dr Jianhua Gu of the HMRI Microscopy-SEM/AFM core on SEM imaging and Mr Carlos Favela for his help on Confocal imaging. The authors acknowledge financial support from the following sources: NIH U54CA151668-01, NIH 1R21CA190024-01, DOD W81XWH-12-1-0414, DOD W81XWH-10-2-0125, National Natural Science Foundation of China 81571791, and Houston Methodist Research Institute.

Notes and references

1 X. Y. Cheng, S. B. Lowe, P. J. Reece and J. J. Gooding, *Chem. Soc. Rev.*, 2014, **43**, 2680–2700.
2 Y. L. Wang, T. Y. Wang, P. M. Da, M. Xu, H. Wu and G. F. Zheng, *Adv. Mater.*, 2013, **25**, 5177–5195.
3 J. H. Park, L. Gu, G. von Maltzahn, E. Ruoslahti, S. N. Bhatia and M. J. Sailor, *Nat. Mater.*, 2009, **8**, 331–336.
4 V. R. Almeida, C. A. Barrios, R. R. Panepucci and M. Lipson, *Nature*, 2004, **431**, 1081–1084.
5 A. S. Liu, R. Jones, L. Liao, D. Samara-Rubio, D. Rubin, O. Cohen, R. Nicolaescu and M. Paniccia, *Nature*, 2004, **427**, 615–618.
6 T. Baehr-Jones, T. Pinguet, P. Lo Guo-Qiang, S. Danziger, D. Prather and M. Hochberg, *Nat. Photonics*, 2012, **6**, 206–208.
7 I. Staude, A. E. Miroshnichenko, M. Decker, N. T. Fofang, S. Liu, E. Gonzales, J. Dominguez, T. S. Luk, D. N. Neshev, I. Brener and Y. Kivshar, *ACS Nano*, 2013, **7**, 7824–7832.
8 F. A. Zwanenburg, A. S. Dzurak, A. Morello, M. Y. Simmons, L. C. L. Hollenberg, G. Klimeck, S. Rogge, S. N. Coppersmith and M. A. Eriksson, *Rev. Mod. Phys.*, 2013, **85**, 961–1019.
9 S. W. Hwang, H. Tao, D. H. Kim, H. Y. Cheng, J. K. Song, E. Rill, M. A. Brenckle, B. Panilaitis, S. M. Won, Y. S. Kim, Y. M. Song, K. J. Yu, A. Ameen, R. Li, Y. W. Su, M. M. Yang, D. L. Kaplan, M. R. Zakin, M. J. Slepian, Y. G. Huang, F. G. Omenetto and J. A. Rogers, *Science*, 2012, **337**, 1640–1644.
10 H. Wu, G. Chan, J. W. Choi, I. Ryu, Y. Yao, M. T. McDowell, S. W. Lee, A. Jackson, Y. Yang, L. B. Hu and Y. Cui, *Nat. Nanotechnol.*, 2012, **7**, 309–314.
11 B. F. P. McVey and R. D. Tilley, *Acc. Chem. Res.*, 2014, **47**, 3045–3051.
12 E. Tasciotti, X. W. Liu, R. Bhavane, K. Plant, A. D. Leonard, B. K. Price, M. M. C. Cheng, P. Decuzzi, J. M. Tour, F. Robertson and M. Ferrari, *Nat. Nanotechnol.*, 2008, **3**, 151–157.
13 F. Priolo, T. Gregorkiewicz, M. Galli and T. F. Krauss, *Nat. Nanotechnol.*, 2014, **9**, 19–32.
14 X. Cheng, E. Hinde, D. M. Owen, S. B. Lowe, P. J. Reece, K. Gaus and J. J. Gooding, *Adv. Mater.*, 2015, **27**, 6144–6150.
15 Y. L. Zhong, F. Peng, F. Bao, S. Y. Wang, X. Y. Ji, L. Yang, Y. Y. Su, S. T. Lee and Y. He, *J. Am. Chem. Soc.*, 2013, **135**, 8350–8356.
16 M. Montalti, A. Cantelli and G. Battistelli, *Chem. Soc. Rev.*, 2015, **44**, 4853–4921.
17 J. P. Wilcoxon, G. A. Samara and P. N. Provencio, *Phys. Rev. B: Condens. Matter*, 1999, **60**, 2704–2714.
18 R. K. Baldwin, K. A. Pettigrew, J. C. Garno, P. P. Power, G. Y. Liu and S. M. Kauzlarich, *J. Am. Chem. Soc.*, 2002, **124**, 1150–1151.
19 J. R. Heath, *Science*, 1992, **258**, 1131–1133.
20 L. Mangolini, *J. Vac. Sci. Technol., B*, 2013, 31.
21 Y. L. Zhong, X. T. Sun, S. Y. Wang, F. Peng, F. Bao, Y. Y. Su, Y. Y. Li, S. T. Lee and Y. He, *ACS Nano*, 2015, **9**, 5958–5967.

 This journal is © The Royal Society of Chemistry 2016

Published on 28 July 2016. Downloaded by University of Texas Libraries on 11/21/2018 5:05:31 PM.

22 M. L. Mastronardi, F. Maier-Flaig, D. Faulkner, E. J. Henderson, C. Kubel, U. Lemmer and G. A. Ozin, *Nano Lett.*, 2012, **12**, 337–342.
23 A. G. Cullis, L. T. Canham and P. D. J. Calcott, *J. Appl. Phys.*, 1997, **82**, 909–965.
24 K. Huang, W. L. Lu, X. G. Yu, C. H. Jin and D. R. Yang, *Part. Part. Syst. Charact.*, 2016, **33**, 8–14.
25 X. Y. Ji, F. Peng, Y. L. Zhong, Y. Y. Su, X. X. Jiang, C. X. Song, L. Yang, B. B. Chu, S. T. Lee and Y. He, *Adv. Mater.*, 2015, **27**, 1029–1034.
26 Y. He, Z. H. Kang, Q. S. Li, C. H. A. Tsang, C. H. Fan and S. T. Lee, *Angew. Chem., Int. Ed.*, 2009, **48**, 128–132.
27 M. Guan, W. D. Wang, E. J. Henderson, O. Dag, C. Kubel, V. S. K. Chakravadhanula, J. Rinck, I. L. Moudrakovski, J. Thomson, J. McDowell, A. K. Powell, H. X. Zhang and G. A. Ozin, *J. Am. Chem. Soc.*, 2012, **134**, 8439–8446.
28 F. Deubel, M. Steenackers, J. A. Garrido, M. Stutzmann and R. Jordan, *Macromol. Mater. Eng.*, 2013, **298**, 1160–1165.
29 X. D. Pi, T. Yu and D. R. Yang, *Part. Part. Syst. Charact.*, 2014, **31**, 751–756.
30 M. Dasog, J. Kehrle, B. Rieger and J. G. C. Veinot, *Angew. Chem., Int. Ed. Engl.*, 2016, **55**, 2322–2339.
31 S. Mitra, S. Cook, V. Svrcek, R. A. Blackley, W. Zhou, J. Kovac, U. Cvelbar and D. Mariotti, *J. Phys. Chem. C*, 2013, **117**, 23198–23207.
32 C. P. F. Rousseau, J. Garcia and M. Popallt, *Chem. Mater.*, 1995, **7**, 828–839.
33 A. Nishimura, S. Harada and T. Uchino, *J. Phys. Chem. C*, 2010, **114**, 8568–8574.
34 T. Brankova, V. Bekiari and P. Lianos, *Chem. Mater.*, 2003, **15**, 1855–1859.
35 B. Qiao, T. J. Wang, H. Gao and Y. Jin, *Appl. Surf. Sci.*, 2015, **351**, 646–654.
36 J. Wang, D. X. Ye, G. H. Liang, J. Chang, J. L. Kong and J. Y. Chen, *J. Mater. Chem. B*, 2014, **2**, 4338–4345.
37 X. D. Zhang, X. K. Chen, S. Q. Kai, H. Y. Wang, J. J. Yang, F. G. Wu and Z. Chen, *Anal. Chem.*, 2015, **87**, 3360–3365.
38 F. G. Wu, X. D. Zhang, S. Q. Kai, M. Y. Zhang, H. Y. Wang, J. N. Myers, Y. X. Weng, P. D. Liu, N. Gu and Z. Chen, *Adv. Mater. Interfaces*, 2015, **2**, 1500360.
39 C. Liu, Z. Zhao, R. L. Zhang, L. Yang, Z. Y. Wang, J. W. Yang, H. H. Jiang, M. Y. Han, B. H. Liu and Z. P. Zhang, *J. Phys. Chem. C*, 2015, **119**, 8266–8272.
40 A. Gil and P. Grange, *Colloids Surf., A*, 1996, **113**, 39–50.
41 A. Virga, P. Rivolo, E. Descrovi, A. Chiolerio, G. Digregorio, F. Frascella, M. Soster, F. Bussolino, S. Marchio, F. Geobaldo and F. Giorgis, *J. Raman Spectrosc.*, 2012, **43**, 730–736.
42 K. Q. Peng, J. J. Hu, Y. J. Yan, Y. Wu, H. Fang, Y. Xu, S. T. Lee and J. Zhu, *Adv. Funct. Mater.*, 2006, **16**, 387–394.
43 S. Schunemann, G. Dodekatos and H. Tuysuz, *Chem. Mater.*, 2015, **27**, 7743–7750.
44 D. Radziuk and H. Mohwald, *ACS Nano*, 2015, **9**, 2820–2835.
45 L. D. Carlos, R. A. S. Ferreira, R. N. Pereira, M. Assuncao and V. D. Bermudez, *J. Phys. Chem. B*, 2004, **108**, 14924–14932.
46 A. M. Jakob and T. A. Schmedake, *Chem. Mater.*, 2006, **18**, 3173–3175.
47 L. Wang, M. C. Estevez, M. O'Donoghue and W. H. Tan, *Langmuir*, 2008, **24**, 1635–1639.
48 W. H. Green, K. P. Le, J. Grey, T. T. Au and M. J. Sailor, *Science*, 1997, **276**, 1826–1828.
49 A. Shiohara, S. Hanada, S. Prabakar, K. Fujioka, T. H. Lim, K. Yamamoto, P. T. Northcote and R. D. Tilley, *J. Am. Chem. Soc.*, 2010, **132**, 248–253.
50 J. H. Warner, H. Rubinsztein-Dunlop and R. D. Tilley, *J. Phys. Chem. B*, 2005, **109**, 19064–19067.
51 J. Salonen, A. M. Kaukonen, J. Hirvonen and V. P. Lehto, *J. Pharm. Sci.*, 2008, **97**, 632–653.
52 M. Y. Abdalla, *Jordan J. Biol. Sci.*, 2011, **4**, 119–124.
53 X. D. Zhang, F. G. Wu, P. D. Liu, N. Gu and Z. Chen, *Small*, 2014, **10**, 5170–5177.
54 L. A. Herzenberg, S. C. DeRosa, J. G. Dubs, M. Roederer, M. T. Anderson, S. W. Ela, S. C. Deresinski and L. A. Herzenberg, *Proc. Natl. Acad. Sci. U. S. A.*, 1997, **94**, 1967–1972.
55 T. Shiomi, H. Tsutsui, H. Matsusaka, K. Murakami, S. Hayashidani, M. Ikeuchi, J. Wen, T. Kubota, H. Utsumi and A. Takeshita, *Circulation*, 2004, **109**, 544–549.
56 R. R. Deng, X. J. Xie, M. Vendrell, Y. T. Chang and X. G. Liu, *J. Am. Chem. Soc.*, 2011, **133**, 20168–20171.
57 L. J. Huang, M. He, B. B. Chen and B. Hu, *J. Mater. Chem. A*, 2015, **3**, 11587–11595.
58 J. Zhang and S. H. Yu, *Nanoscale*, 2014, **6**, 4096–4101.
59 F. Wang, W. Li, X. L. Feng, D. P. Liu and Y. Zhang, *Chem. Sci.*, 2016, **7**, 1867–1873.
60 S. E. Lehman, Y. Tataurova, P. S. Mueller, S. V. S. Mariappan and S. C. Larsen, *J. Phys. Chem. C*, 2014, **118**, 29943–29951.
61 R. S. Reid, *J. Chem. Educ.*, 1989, **66**, 344–345.
62 Y. Y. Su, X. P. Wei, F. Peng, Y. L. Zhong, Y. M. Lu, S. Su, T. T. Xu, S. T. Lee and Y. He, *Nano Lett.*, 2012, **12**, 1845–1850.
63 Y. H. Yi, J. H. Deng, Y. Y. Zhang, H. T. Li and S. Z. Yao, *Chem. Commun.*, 2013, **49**, 612–614.